Cathode-less RF plasma thruster design and optimisation for an atmosphere-breathing electric propulsion (ABEP) system

Cathode-less RF Plasma Thruster Design and Optimisation for an Atmosphere-Breathing Electric Propulsion (ABEP) System

Abstract

Atmosphere-breathing electric propulsion (ABEP) is a concept that ingests residual atmospheric gases as a source of propellant for an electric thruster, removing the need for onboard propellant storage. This would enable continuous low-thrust drag compensation, extending the lifetime of spacecraft in Very-Low Earth Orbit (VLEO); <250 km. VLEO is an appealing region for spacecraft operations, enabling new remote sensing missions with improved radiometric performance and spatial resolution, whilst reducing size, mass and power requirements, as well as mission cost. A preliminary design review and optimisation is therefore conducted for an ABEP system that uses the cathode-less radio frequency (RF) plasma thruster from Technology for Innovation & Propulsion (T4i) S.p.A. This removes the issue of thruster erosion by means of magnetic confinement and offers reduced susceptibility to varying atmospheric composition. A semi-empirical oxygen-nitrogen global source model (GSM) has been developed which considers the volume-averaged flux, momentum, and energy balance of the RF discharge. This includes a detailed chemistry model for the complex electron-molecular reactions and energy-loss channels of air plasma in the ionisation chamber. The GSM is coupled to an analytical model of flux balance for an air intake, verified by Direct Simulation Monte-Carlo (DSMC) simulation, to consider its design for maximum collection efficiency. This is then utilised in a robust multi-objective optimisation of the ABEP system, accounting also for spacecraft aerodynamics and power requirements.

Keywords: Atmosphere-Breathing Electric Propulsion (ABEP), Cathode-less RF plasma thruster, Very Low Earth Orbit (VLEO), Global plasma model, Robust optimisation

1. Introduction

Atmosphere-breathing electric propulsion (ABEP) is a concept that ingests residual atmospheric gases as a source of propellant for an electric thruster, removing the need for onboard propellant storage [1]. This would enable continuous low-thrust drag compensation, extending the lifetime of aeronomic satellites in Very-Low Earth Orbit (VLEO); <250 km [2].

VLEO is highly appealing for flexible, high-performing and economical spacecraft operations to deliver low-cost communications and Earth observation data [3]. Ground resolution is directly proportion to altitude; therefore, instrument volume, mass and cost reduces with altitude for the same performance. The radiometric resolution also improves according to the inverse-square of altitude, yielding higher signal-to-noise ratios. VLEO can therefore provide substantial improvements in the performance of Earth remote sensing payloads for applications such as meteorology, oceanic circulation, polar ice, wildfires, agriculture, urban mapping or military surveillance. VLEO satellites also benefit from improved communications latency and link budget, and the launch vehicles can provide greater payload mass fractions [4]. Concerns over the increasing debris population in commercially exploited orbits is also avoided.

Drag-compensated VLEO flight has previously been demonstrated with conventional propellant: The European Space Agency's (ESA) Gravity Field and Steady-State Ocean Circulation Explorer (GOCE) was launched in 2009 [5]. GOCE used a QinetiQ T5(UK-10) ion thruster to compensate for the orbital decay, sustaining an orbital altitude of 250-265km for 55 months before expending its fuel. The Super Low Altitude Test Satellite (SLATS) was launched in 2017 by the Japan Aerospace Exploration Agency (JAXA), with the objectives to understand the effects of high-density atomic oxygen on the satellite and to verify drag-compensation feasibility with a Kiku-8 ion thruster [6]. Subsequently, several ABEP projects have arisen. These include the ESAs RAM-EP (Residual Atmosphere for Maneuvering by Electric Propulsion) [7], JAXA's ABIE (Air-Breathing Ion Engine) [8], the European Commission's AETHER (Atmosphere-breathing Electric THrustER) [9], and Busek Co.'s ABHET (Atmosphere-Breathing Hall Effect Thruster) [10].

However, the presence of reactive chemical species, including atomic oxygen in VLEO, is a lifetime-limiting cause of discharge channel, grid and hollow cathode erosion in conventional electric propulsion systems such as ion and Hall-effect thrusters [9,11]. This self-defeats the purpose of such ABEP systems to extend mission lifetime. Cathode-less electric propulsion (EP) systems, such as the inductive plasma thruster (IPT) of the European Commission's DISCOVERER ABEP program [12], are superior in this regard, making them particularly suitable to ABEP

operations. The REGULUS cathode-less Helicon-based radio frequency (RF) plasma thruster has been under development by Technology for Innovation & Propulsion (T4i) S.p.A. since 2015 [13,14]. The 50 W iodine-fuelled model REGULUS-50-I_2 performed successful in-orbit demonstration in Q1 2021 [15], where it provided VLEO drag-compensation for the GAUSS S.r.l. UniSat-7 satellite-deployer mission [16,17]. More recently, under the EarthNext program funded by the Agenzia Spaziale Italiana, REGULUS-50-I_2 (11 kNs) will station-keep operations in VLEO of an 16U CubeSat for Earth observation. The REGULUS system also includes 150 W class and xenon-fuelled configurations.

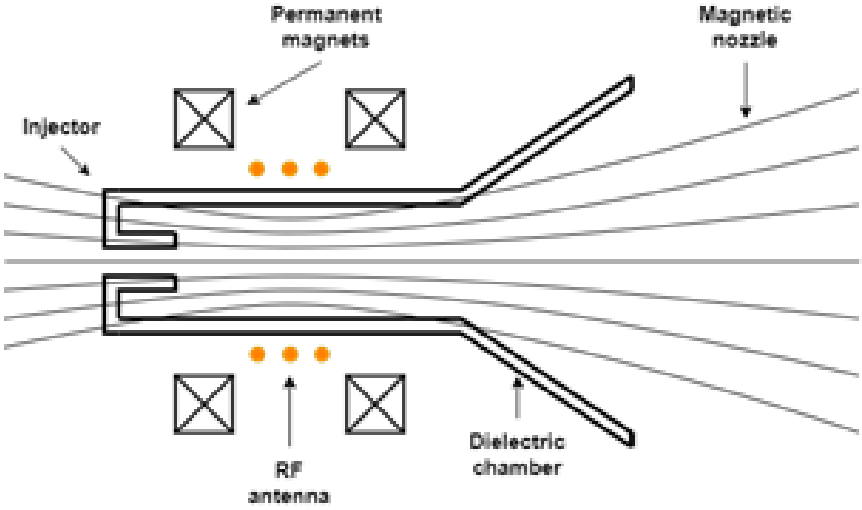

Figure 1: Schematic of cathode-less RF plasma thruster

The principle of the cathode-less RF thruster is illustrated in Fig. 1. Plasma is produced within a source tube using radiofrequency (RF) ionisation, enhanced by a magnetic field which also accelerates the discharge via the magnetic nozzle effect [18]. The result is a series of advantages that lend themselves to VLEO operation: broader propellent compatibility, reduced erosion issues, reduced contamination, low maintenance, enhanced reliability, lightweight and simplified design, as well as the capability for low-density, low-pressure ignition [19]. A preliminary design review and optimisation is therefore conducted for an ABEP system that uses the cathode-less RF thruster technology. This removes the issue of thruster erosion by means of magnetic confinement and offers reduced susceptibility to varying atmospheric composition.

The issue regarding the uncertainty of VLEO conditions, arising from solar weather, thermospheric wind, gas-surface interactions and orbital perturbations is

a critical one. There have been many studies into the feasibility and optimisation of the ABEP systems discussed above [7-10]. But the literature often makes use of representative or average conditions for a singular design point [20,21]. Robust optimisation is indispensable for ensuring the effectiveness, reliability, and cost-efficiency of ABEP systems in VLEO missions. It allows spacecraft to adapt to dynamic environmental conditions and operational uncertainties, thereby enhancing mission success and the long-term sustainability in this critical orbital regime.

To this end, this paper demonstrates the robust optimisation of an ABEP system. A semi-empirical oxygen-nitrogen global source model (GSM) has been developed which considers the volume-averaged flux, momentum, and energy balance of the RF discharge [22]. This includes a detailed chemistry model for the complex electron-molecular reactions and energy-loss channels of air plasma in the ionisation chamber. The GSM is coupled to an analytical panel model of flux balance for an air intake, a panel method for satellite aerodynamics as well as power and thermal models. While similar models have been described in the literature previously, it is stressed that the novel aspect of this work is the application of robust optimisation methodology to ABEP design, as well as the performance analysis of the REGULUS cathode-less RF thruster under varying environmental conditions in VLEO. A novel air intake concept is also introduced.

2. Orbit and atmospheric variability

2.1. Orbital conditions

Dawn-dusk sun-synchronous orbits (SSO) are considered as to neglect eclipses, and thus allow continuously generated power with solar arrays. These orbital profiles are simulated via a high-accuracy orbit propagator, which considers harmonics of the Earth's gravity up to 18 and provides the inputs for the NRLMSISE-00 atmospheric model at each timestep [23]. For these simulations, the drag is neglected to replicate an idealistic drag-compensating condition, since the requirement here is to only obtain representative atmospheric properties.

In VLEO, the non-sphericity of Earth's gravity has a significant effect, resulting in unavoidable and osculating eccentricity of the orbit. This is significant given that even a small change in altitude yields considerably different atmospheric composition and temperature, placing altered demands on both intake thruster performance.

Fig. 2 (a) displays the orbital altitude variation in VLEO for two simulated SSO's with mean altitudes of 160 and 200 km, over a sample of 30 days. The eccentricity due to non-spherical gravity is indicated by the immediate periapsis–apoapsis range of 144-181 km and 180-226 km respectively; with 30-50 km variations expected, large variations in atmospheric properties and incoming flow speed are inherent.

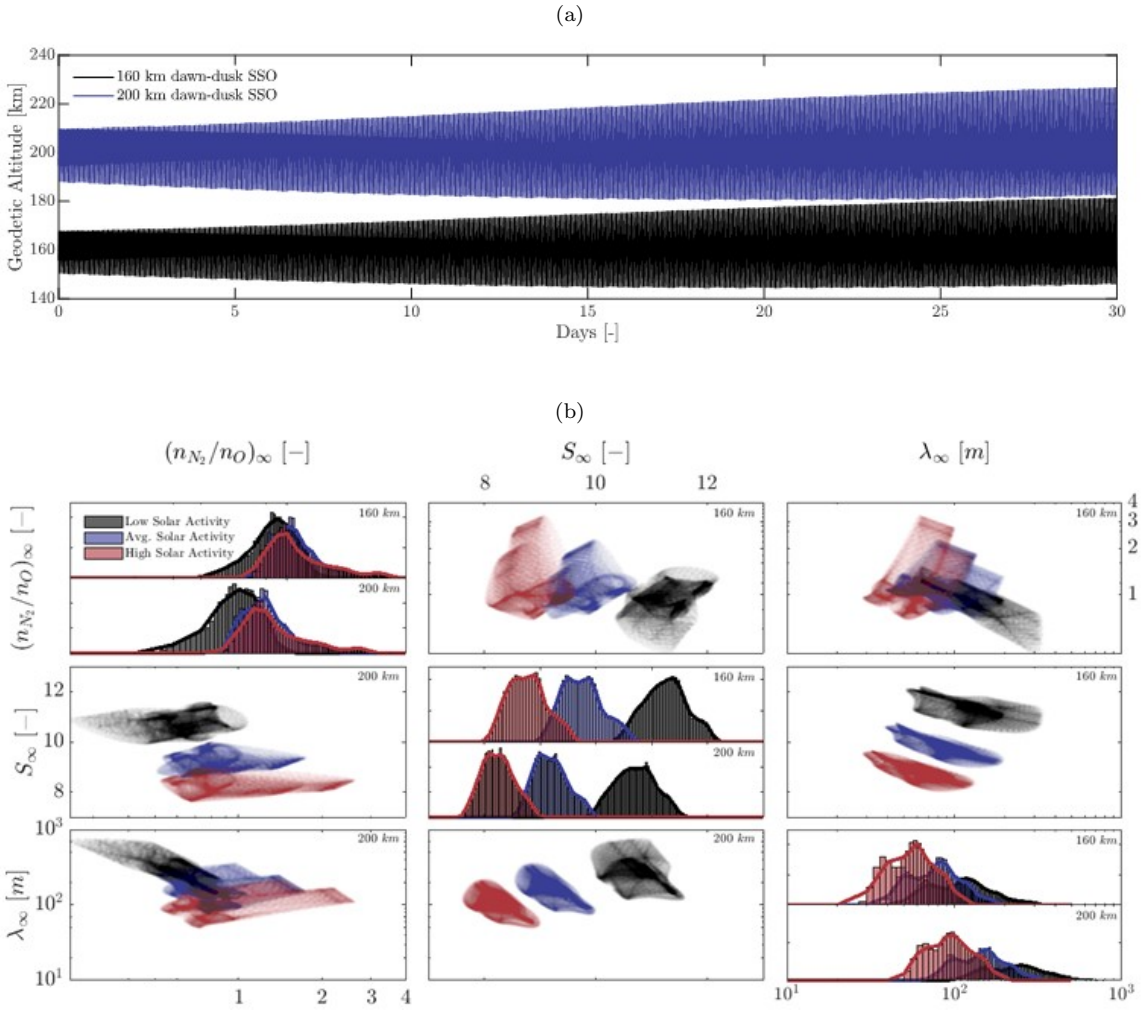

Figure 2: (a) Orbital altitude variation over a 30 day period at 160 and 200 km mean-altitude SSO. (b) Multivariate distributions of VLEO environmental parameters at 160 and 200 km at low, average and high solar activity. The diagonal provides the single variable probability distribution functions

2.2. Atmospheric variability

The NRLMSISE-00 model is used to provide the flow temperature T_∞, total mass density ρ_∞ and number density n_∞ for each atmospheric component. It includes the effect of solar activity, in the form of an input for the 10.7 cm solar radio flux index $F10.7$ and the magnetic A_p index, which are measures of the solar radiation in the

wavelengths that cause atmospheric ionisation and the variation in the daily average of the Earth's magnetic field respectively [23]. The nominal average values are taken here as $F10.7 = 140$, $A_p = 15$, minimum values as $F10.7 = 65$, $A_p = 0$, and maximum values as $F10.7 = 250$, $A_p = 45$.

The primary noise parameters of interest are:

(I) the hypersonic speed ratio,

$$S_\infty = \frac{v_\infty}{\sqrt{\frac{2k_B T_\infty}{\bar{m}_\infty}}}, \tag{1}$$

where v_∞ is the freestream flow velocity along the satellite roll axis (equal to the orbital velocity when neglecting yaw angle), T_∞ is the freestream temperature, $\bar{m}_\infty$ the mean freestream particle mass and k_B is the Boltzmann constant. This is the ratio of the freestream speed to its most probable thermal velocity, having direct effect on intake performance and platform drag.

(II) the composition ratio, n_{N_2}/n_O, of diatomic nitrogen N_2 to atomic oxygen O. Whilst this also effects intake performance and aerodynamic properties, it will mainly effect the performance of the thruster by altering the plasma composition.

(III) the mean free path,

$$\lambda_\infty = \frac{1}{n_\infty \sqrt{2}\pi d^2}, \tag{2}$$

where n_∞ is the freestream number density and d is the representative molecular diameter. This quantifies the effect of gas-phase collisions and the degree of flow rarefaction. Note that it also inversely quantifies the effect of density

In Fig. 2 (b), the multivariate distributions of these noise parameters are illustrated for both the 160 and 200 km dawn-dusk SSO's, and at each level of solar activity. In all the samples considered N_2 and O constitute at least 90% of the gas composition. Their relative composition however varies largely; n_{N_2}/n_O= 0.53-5.12 at 160 km and 0.18-3.17 at 200 km (atomic oxygen is more prevalent at higher altitude).

Because of the higher atmospheric temperature and higher fraction of lighter species, S_∞ is lower at higher altitude and much lower at higher solar activity. Its dependence on species mass provides a strong correlation with n_{N_2}/n_O. Overall, it varies between 8.7-12.9 and 7.8-11.3 for 160 and 200 km respectively. This is challenging for the operating range of intakes.

The mean free path λ_∞ has a dynamic range of about one order of magnitude at each altitude. It can be as low as 20 m in the 160 km high solar activity case and as high as 750 m in the 200 km low solar activity case. For a platform on the order

of 1 m, this does mean the flow is safely in the free molecular regime. However, its large variance-especially at low solar activity-raises the issue of required geometric robustness in intake and aerodynamic design. It is judicious to mention that the yaw angle and angle of attack of the incoming flow will also vary greatly in VLEO due to thermospheric winds and spacecraft attitude. However, in the first analysis here, the flow is considered perfectly aligned and the effects left to detailed design requiring the use of DSMC simualtions.

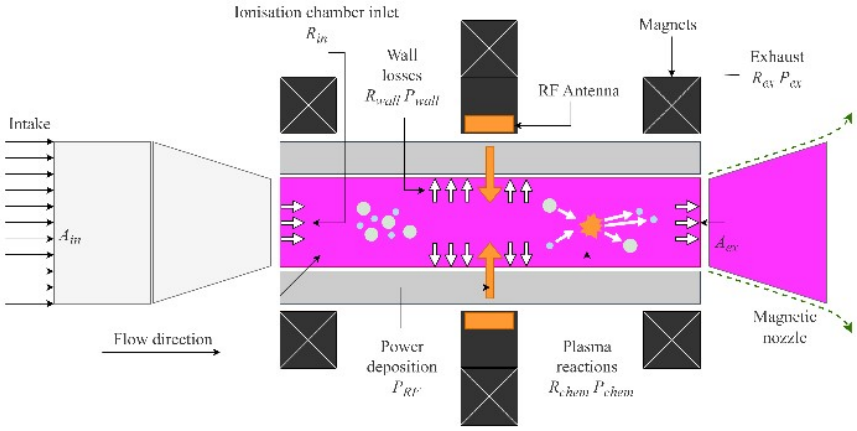

Figure 3: Terms of the global source model

3. Sub-System models

3.1. Cathode-less RF thruster

To predict the air species population densities and the electron temperature within the source tube, a 0D Global Source Model (GSM) has been adopted [22,24-26]. The plasma production is assumed to occur only within the cylindrical region of the source tube, with an open end for the outlet. The magnetic field is considered uniform and perfectly aligned with the thruster axis; the effect of cusps is accounted for through empirical relations [22,26]. The species flux balance and electron power balance respectively are then given as,

$$\frac{dn_k}{dt} = R^k_{chem} - R^k_{wall} + R^k_{in} - R^k_* \tag{3}$$

$$\frac{d}{dt}\left(\frac{3}{2}n_e\langle T_e\rangle\right) = P'''_a - P'''_{chem} - P'''_{wall} + P'''_{in} - P'''_* \tag{4}$$

where n_k is the number density of the k-th species, and $\langle T_e \rangle$ is the global average electron temperature. R^k_{chem} is the term associated to production/loss of the k-th species due to chemical reactions, R^k_{wall} the same for wall surfaces losses/recombination, R^k_{in} is the source term of the air injected into the source tube (it is a direct function of the intake collection efficiency η_c), and R^k_* is the species sonic flux exiting the discharge, into the magnetic nozzle. P'''_{chem},P'''_{wall},P'''_{in},P'''_* are the equivalent volumetric power density terms for the electron species. P'''_a is the volumetric power density absorbed into the plasma from the RF antenna; Accounting for impedance mismatching. the coupling efficiency is taken to be constant $\eta_{RF} = P_a/P_{RF} = 0.8$ from previous measurements [24-27]. The thrust is then obtained analytically as [27],

$$T = \sum_{k=1}^{K} \left(T^k_p + T^k_{gas} \right) \tag{5}$$

$$T^k_p = T^k_0 \frac{\mathcal{M}^2_{det} + 1}{2\mathcal{M}_{det}} \tag{6}$$

$$T^k_{gas} = \dot{m}^k_{ex} \bar{v}_k \left(1 + \frac{k_B T^k_g}{m_k \bar{v}^2} \right) \tag{7}$$

where Eq. 5 is the summation of the plasma T_p and neutral gas T_g contributions, $\mathcal{M}_{det}$ is the magnetic Mach number at detachment (solved numerically according to Lafleur [28]), $\bar{v}$ is the neutral sound speed, and T_g is the neutral gas temperature. The pre-acceleration plasma thrust is $T^k_0 = 2\beta_k e n_k \langle T_e \rangle A_{out}$, with β an empirical parameter that accounts for the non-uniformity of the plasma [22,26].

In this work, the considered species are electron, atomic, and molecular neutral species, namely, N, N_2, O, O_2, NO, N_2 O, NO_2, excited state, and single-charged atomic and molecular ions. Regarding the chemistry model, the reactions that were included, listed in Table 1, are elastic scattering, excitation, ionisation and neutralisation, molecular dissociation, attachment and detachment, dissociative neutralisation and ionisation, and charge exchange. The relevant reaction cross-sections were recovered from the Biagi database [29]. In total, over 130 reaction pathways are present. Therefore, to reduce some of the computational burden, atomic and molecular excitation states were reduced using the lumping methodology laid down by Souhair et al. [30,31]. In the GSM, the reaction rates K involving electrons are calculated assuming a Maxwellian distribution of electron impact energy E_e,

$$K(T_e) = \sqrt{\frac{8}{\pi m_e T_e^3}} \int_{E^*}^{\infty} E_e \sigma \left(E_e \right) e^{-\frac{E_e}{T_e}} dE_e \tag{8}$$

Table 1: Air chemistry included in the GSM

Type	Reaction	Species
Atomic Elastic Scattering	$e + A \rightarrow A + e$	N, O
Atomic Excitation	$e + A \rightarrow A^* + e$	N, O
Atomic Ionization	$e + A \rightarrow A^+ + 2e$	N, O
Atomic Neutralization	$e + A^+ \rightarrow A$	N, O
Atomic Attachment	$e + A \rightarrow A$	O_2, NO, NO_2
Molecular Elastic Scattering	$e + AB \rightarrow AB + e$	N_2, O_2
Molecular Excitation	$e + AB \rightarrow AB^* + e$	N_2
Molecular Ionization	$e + AB \rightarrow AB^+ + 2e$	N_2, O_2
Molecular Dissociative Ionization	$e + AB \rightarrow A + B^+ + 2e$	O_2
Molecular Dissociative Attachment	$e + AB \rightarrow A + B^-$	O_2, NO_2, N_2O
Molecular Dissociation	$e + AB \rightarrow A + B + e$	N_2, O_2
Molecular Neutralization	$e + AB^+ \rightarrow AB$	N_2, O_2, NO
Molecular Attachment	$e + AB \rightarrow AB^-$	O_2, NO, NO_2
Molecular Dissociative Neutralization	$e + AB^+ \rightarrow A + B$	N_2, O_2, NO, NO_2, N_2O
Charge Exchange	$A^+ + B \rightarrow A + B^+$	N, $N_2, O, O_2, NO, NO_2, N_2O$
Mutual Neutralization	$A^+ + B^- \rightarrow A + B$	N, N_2, O, O_2, NO, NO_2, N_2O
Recombination	$A + B \rightarrow AB$	N, N_2, O, O_2, NO
Ion Recombination	$A + B^+ \rightarrow AB^+$	N, O, NO
Associative Detachment	$A + B^- \rightarrow AB + e$	O, O_2, NO, NO_2
Associative Neutralization	$A^+ + B^- \rightarrow AB$	N, N_2, O, O_2, NO

where E^* and σ are the energy threshold and collision cross sections respectively. Before proceeding, the reaction processes and rate coefficients can already be used to gain important insight into the application of air as propellant. A metric sometimes used for plasma discharges is the collisional energy loss which represents the average energy expended to produce an electron–ion pair when considering all collisional processes, the ion-cost. This is given as,

$$\epsilon_c(T_e) = \frac{\sum_{i=1}^{I} K_i(T_e) E_i^*(T_e)}{\sum_{j=1}^{J} K_{j(0\rightarrow+)}(T_e)} \tag{9}$$

where the numerator represents the sum of the collisional energy loss rate of all processes, and the denominator is instead the loss rate only of ion-producing reactions (ionisation and dissociation).

Fig. 4 shows this ion-cost as a function of electron temperature in the range expected for the ABEP thruster. It can immediately be seen that whether the air plasma is made up largely of N_2 or O has a large effect on the collisional energy loss and shifts the cross-over point between the traditional Xe curves by about 5 eV.

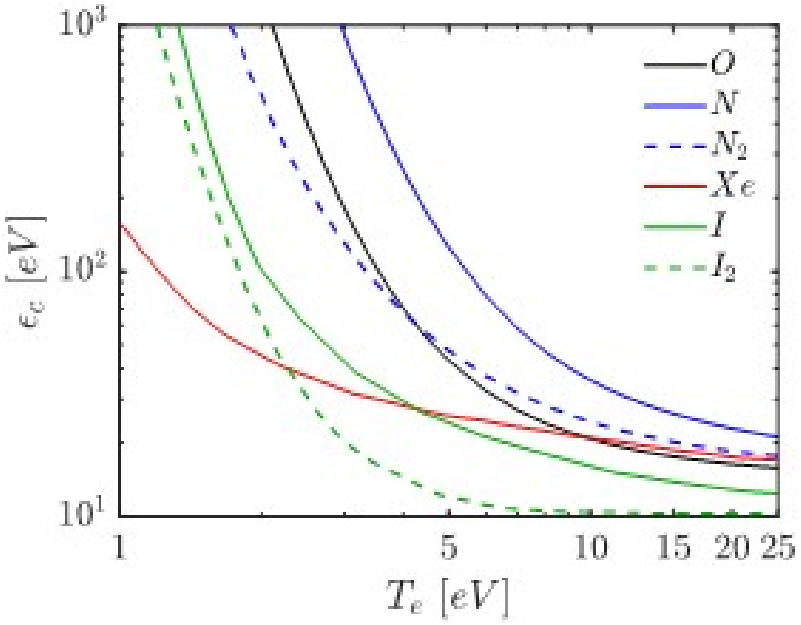

Figure 4: Effective collisional energy loss per electron–ion pair as a function of electron temperature

Although the energy loss in pure N_2 and O plasmas is significantly higher than both Xe and I at low electron temperatures, above about 10 eV the energy loss of N_2 and O is comparable to Xe in the region of 15-18 eV. However, this remains about 5 eV greater than iodine. This is due to the different collision cross-sections, reaction process, and inelastic energy thresholds.

While the electron temperature in air compared to xenon or iodine plasma discharges is not in general equal, it is expected to be similar [32]. Fig. 4 therefore indicates that using air can lead to lower collisional energy losses if the electron temperature is sufficiently high and there is a high concentration of O. Indeed, the cross-over point of O and N_2 exists at 4 eV, representing a key condition when factoring in composition ratio in design (although in practice, such low-temperatures are unlikely to meet thrust requirements). Since most atmospheric operating conditions have comparable levels of atomic oxygen and nitrogen, the effective energy loss can be expected to sit somewhere between the two curves.

3.2. Intake

While several literature works have yielded impressive performance from specularly reflecting intakes [21,33], it is conservative practice to consider the gas-surface interactions in VLEO to be diffuse. A classic passive intake with entrance ducts is

therefore considered here. Extending the work of other authors [20,34], a quasi-2D panel-like method is derived to estimate the performance of the intake. The flux of gas from the freestream is approximated as hypersonic ($S_\infty \gg 1$) and is free molecular everywhere; particles considered to have struck the thermalization chamber have a Maxwellian distribution at the temperature of the walls T_w and the surface reflections are fully diffusive. When considering the flow through the intake, the three determinate fluxes can be expressed as,

$$R_{in} = n_\infty v_\infty A_{in} \Theta_{in} \tag{10}$$

$$R_{out} = \frac{1}{4} n_{out} v_{th} A_{out} \Theta_{out} \tag{11}$$

$$R_{back} = \frac{1}{4} n_{back} v_{th} A_{in} \Theta_{back} \tag{12}$$

where Θ are the free-molecular transmittances and v_{th} is the thermal speed. To acquire the values of the required Θ, the intake is divided up into panels in both the axial and radial dimensions; one set for the ducted section and another for the chamber. The individual Θ for each element, along with its Clausing factor Θ^* (the transmittance for thermalised flow), is found from the results of DSMC simulations presented in the literature [20]. They are exclusively functions of S_∞ and the segment aspect ratio. For multiple segments in series arrangement, the combined transmittance can then be found by superposition via Eq. 13 for k elements:

$$\Theta_{1\ldots k} = \prod_{i=1}^{k} \Theta_i + \sum_{m=1}^{k} \left[\left(\prod_{i=1}^{m-1} \Theta_i \right) (1 - \Theta_m) \left(\prod_{j=m}^{k} (1 - \Theta_j^*) \Theta_m^* \right) \sum_{n=0}^{N} \left(\prod_{j=m}^{k} (1 - \Theta_j^*) \right) \right]^n \tag{13}$$

The collection efficiency of the intake may then be found as,

$$\eta_c = \frac{R_{out}}{n_\infty v_\infty A_{in} + \frac{\Theta_{in}\Theta_{out}}{\Theta_{back} + \frac{A_{out}}{A_{in}}\Theta_{out}} \frac{A_{out}}{A_{in}}}, \tag{14}$$

and the compression ratio as,

$$\nu = n_{out}/n_\infty = 2\sqrt{\pi} S_\infty \sqrt{\frac{T_\infty}{T_w}} \frac{\Theta_{in}}{\Theta_{back} + \frac{A_{out}}{A_{in}}\Theta_{out}} \tag{15}$$

From the perspective of the balance model, ionised gas exiting the thruster, through the MN, is effectively equivalent to the direct transmittance of those inflowing neutral particles through the source tube. Taking the unionised propellant

fraction to be small, then the value of Θ_{out} is considered approximately equal to the thruster mass utilization efficiency η_u, which is an output of the GSM. The value of T_w is calculated according to the heating from the onset flow as it assumes stagnation conditions with all particles led adiabatically to rest at the intake surfaces, neglecting conduction through the wall

$$T_w = \left(\frac{\rho_\infty v_\infty \left(\frac{v_\infty^2}{2} + c_p T_\infty \right)}{\varepsilon_r \sigma_B} \right)^{1/4} \tag{16}$$

where ϵ_r is the emissivity (assumed to be 0.5), c_p the specific heat capacity at constant pressure (which depends on the composition) and σ_B is the Stefan-Boltzmann constant.

3.3. Aerodynamics

In the free-molecular flow regime, the air is assumed to act as individual particles and forces imparted on the body are calculated from the momentum transfer of particle collisions. The panel method of Sentman is therefore used to evaluate the drag of the satellite platform [35]. A single accommodation coefficient α_w is used to quantify energy transfer to the surface and is taken to be 0.9. Diffuse re-emission is assumed, which is correct for typical VLEO conditions. The pressure and shear stress coefficients of each panel are given by,

$$\begin{aligned} C_p = &\left(\cos^2(\delta) + \frac{1}{2S_\infty^2} \right) (1 + erf(S_\infty \cos(\delta))) + \frac{\cos(\delta)}{S_\infty \sqrt{\pi}} e^{-S_\infty^2 \cos^2(\delta)} \\ &+ \frac{1}{2} \sqrt{\frac{2}{3} \left(1 + \alpha_w \left(\frac{T_w}{T_\infty} - 1 \right) \right)} \left[\sqrt{\pi} \cos(\delta) erf(S \cos(\delta)) + \frac{1}{S_\infty} e^{-S_\infty^2 \cos^2(\delta)} \right] \end{aligned} \tag{17}$$

$$C_\tau = \sin(\delta) \cos(\delta) \left(1 + erf(S_\infty \cos(\delta))\right) + \frac{\sin(\delta)}{S_\infty \sqrt{\pi}} e^{-S_\infty^2 \cos^2(\delta)} \tag{18}$$

with δ the angle between the oncoming flow and panel surface normal vector. The drag of each panel is then,

$$F_d = \frac{1}{2} \rho_\infty v_\infty^2 A_{ref} C_d. \tag{19}$$

The drag coefficient being given by $C_d = C_p cos(\delta) + C_\tau sin(\delta)$ and A_{ref} is the projected area of the panel. The total platform drag is then taken to be,

$$F_D = F_D^{bus} + F_D^{array} + F_D^{intake}(1 - \eta_c) + \eta_c A_{in} \rho_\infty v_\infty^2. \tag{20}$$

Where $F_D = \sum F_d$ is the sum contributions of the panel decomposition as per Eqs. 17-19 and is separated into the satellite bus, solar array and intake (frontal) contributions. The latter is multiplied by $1 - \eta_c$ due to the fraction of air which does not pass through the intake. The final term accounts for the stagnation of the intake air for thermalisation.

3.4. Power

The satellite solar arrays are modelled to represent the increased solar array area required for generating a higher thrust, due to the corresponding thruster power. The array collecting faces are considered to be perpendicular to the spacecraft trajectory since SSOs are used here. A larger solar array therefore only increases the shear drag (pressure drag negligible) and this limits the operating power. While, in practice, the dawn-dusk SSO's considered here may experience eclipses on the order of 10 minutes, it is assumed the arrays are under continuous solar flux. The beginning-of-life power density of the arrays is taken to be,

$$P_{BOL} = \eta_s G_{SC} I_d \tag{21}$$

where G_{SC}= 1367 Wm^{-2} is the solar constant and η_s and I_d are the panel efficiency and inherent degradation. They are taken as 0.3 and 0.8 respectively, representative of state-of-the-art GaAs arrays. The end-of-life power is then given by,

$$P_{EOL} = P_{BOL}(1 - Y)^{SCL}. \tag{22}$$

Here, Y is the per-year panel degradation, and is 0.0275 for VLEO. SCL is the mission lifetime, taken as 10 yrs. In all, P_{EOL} is about 60% that of the ideal power $\eta_s G_{SC}$. The panel area required (from the RF antenna power P_{RF}) is thus,

$$A_s = \frac{SF \cdot P_{RF}}{P_{EOL}} \tag{23}$$

The term SF is a safety factor to account for other sub-system power and is 1.2. Note, that since this is the array area required to generate the necessary power and only one array side is exposed to solar flux, the actual shear area contributing to drag is in fact $2\left(A_s - A_{bus}^{'}\right)$, where $A_{bus}^{'}$ is considered as the projected area of a body-mounted array of solar cells on the satellite bus.

3.5. Optimisation method

A multi-objective surrogate optimisation algorithm is chosen for the design of the ABEP system. While the GSM is not as computationally intensive as fluid or PIC methods, a function evaluation time of several seconds still yields heavy computational times. The surrogate model approximates the objective function (the sub-system models) as a 'black box' using carefully selected observations of the original function and implementing effective interpolation between these sites [36]. By carefully selecting and tuning the components of the surrogate model it should be possible to minimize the number of samples that are needed to fully explore a given design space. These models approximate the behaviour of the actual system, guiding the search for optimal solutions and aiding decision-makers in navigating trade-offs.

The core of the methodology lies in multi-objective optimization, which navigates the decision variable space to discover a set of Pareto-optimal solutions. These solutions depict the intricate balance between competing objectives, forming a Pareto front. The algorithm iteratively refines the surrogate-based objectives, guiding the search towards the Pareto front. Following convergence, a suite of Pareto-optimal solutions is attained, presenting decision-makers with a comprehensive spectrum of trade-offs.

Further to this, robust optimization, employing the Taguchi Signal-to-Noise Ratio (SNR) methodology [37], is a valuable approach in engineering and scientific research for enhancing the resilience and performance of systems in the presence of variability and uncertainty. This methodology, rooted in quality engineering principles, enables systematic investigation in how variations in input parameters impact the quality or performance of a system [38]. By quantifying the effects of variability using the SNR, optimal settings can be identified that minimize sensitivity to noise factors while maximizing desired outcomes. This robust optimization framework is particularly beneficial to VLEO where achieving consistent and high-quality performance is paramount in the face of inherent variability. For so-termed 'larger-is-better' problems, the SNR can be written as,

$$S/N = 10log_{10}\left(\frac{1}{n}\sum_{i=1}^{n}\alpha_i\left(\frac{1}{y_i}\right)^2\right) \tag{24}$$

where y_i is the result of the objective function evaluated at the i-th condition of the noise variables and α_i is the weighting of noise variable distribution. This weighting comes directly from the multivariate distributions illustrated in Fig. 2 (b).

4. Results

4.1. Setup

For this initial feasibility study, the ABEP system is treated as a standalone nacelle-like element prior to spacecraft integration. Thus, the chosen optimisation variable here is the product of the collection efficiency η_c and thrust efficiency,

$$\eta_t = \frac{T^2}{2\dot{m}_{out} P_a} \tag{25}$$

This gives an optimisation problem of the form,

$$\max_{\underline{\mathbf{x}} \epsilon \mathcal{R}} \left[f_1(\underline{\mathbf{x}}), f_2(\underline{\mathbf{x}}) \right]^T, \tag{26}$$

$$f_1(\underline{\mathbf{x}}) = \overline{\eta_c \eta_t} \tag{27}$$

$$f_2(\underline{\mathbf{x}}) = -10 log_{10} \left(\frac{1}{n} \sum_{i=1}^{n} \alpha_i \left(\frac{1}{(\eta_c \eta_t)_i} \right)^2 \right) \tag{28}$$

where $\underline{\mathbf{x}}$ is the design variable vector. It is noted that the optimisation deals specifically with the on-orbit average values of $\bar{\eta}_c$ and $\bar{\eta}_t$, but that these values change in time according to the orbital propagation according to the required operating condition of the thruster and inflow conditions experienced by the intake. It is then these temporal values that feed into the calculation of robustness. The design variables and their bounds are listed in Table 2. They include the aspect ratios, defined as length-to-radius, of the intake ducts, intake chamber and thruster source tube, the intake area ratio, the radius of the source tube, and the minimum and maximum operating powers.

There are three additional non-linear constraints, that is that $T/D > 1$, $\dot{m}_{out} > 0.05$ mg/s and $\langle T_e \rangle < 30$ eV. This is the thrust-to-drag breakeven condition, minimum mass flow rate for ignition and thermal limitation respectively. All three constraints are evaluated at the minimum and maximum freestream inflow conditions per function evaluation. Note, regarding minimum $\dot{m}_{out}$, that this physically corresponds to a minimum neutral density under the RF antenna, within the source tube, required for ionisation. Considering the model takes the neutral flow as thermalised as it enters the source region, minimum inflow is thus equivalent to minimum density ignition constraints and the value of 0.05 mg/s comes directly from the vast experience of REGULUS experimental campaigns [13-17]. For the preliminary analysis considered

Table 2: Design variables and bounded constraints

Design variable	Lower bound	Upper bound
AR_{duct}	0.5	25
$AR_{chamber}$	0.5	25
$A_{\text{in}}/A_{\text{out}}$	1	20
R_{out} [m]	0.01	0.2
$L_{\text{thruster}}/R_{\text{out}}$	1	7
P_{min} [W]	50	1000
P_{max} [W]	50	1000

here, it is assumed that the ionisation is stable with respect to VLEO environmental disturbances that may propagate through the intake.

With regards to the noise variables, the distributions of S_∞, $(n_{N_2}/n_O)_\infty$ and λ_∞ given in Fig. 1 (b) are reduced to a discrete $5 \times 5 \times 5$ weighted distribution, to limit the number of evaluations for SNR. Note that since only S_∞, $(n_{N_2}/n_O)_\infty$ impacts the results of the GSM- the most expensive element of the overall system model in the objective function- the robustness SNR contribution of the GSM need only be evaluated over the 5 samples in that dimension.

The case of the 160 km SSO, at average solar conditions, is henceforth considered.

4.2. Intake performance

Prior to performing the optimisation, the conceptual design of the intake was explored. The three concepts considered are illustrated in Fig. 5. The classical concept involves ducts of constant aspect ratio and is what is widely discussed in the literature of diffuse intakes. Here, alternatively, a variable aspect ratio design is also analysed here. It features multiple duct aspect ratio to increase the effective intake area directly in front of the thruster's source tube with larger radius ducts, while smaller ducts are at the outer perimeter, as it is hypothesised this region is expected to have larger backflow from particles that have thermalised with the chamber walls. An extension to this, is to modify the ducts to form a diverging conical section, thus reducing the drag coefficient. Introducing a conic nose profile reduces the portion of parallel momentum surface-impacting particles lose to the intake, as per Eqs. 17 and 18. Walsh et al. have shown that 21% to 35% reductions in minimum drag are achievable with conic profiles compared with the cylindrical [45].

For a first analysis, the ratio of the outermost duct width to the central duct width was taken as 0.1 and the latter assumed equal to the source tube radius, with a linear

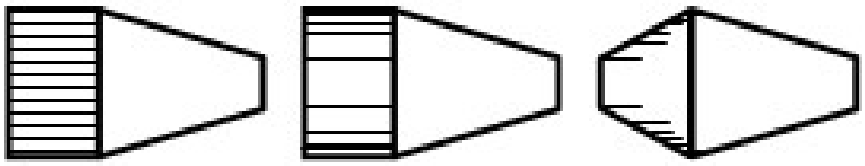

Figure 5: From left to right: Classical, variable AR and variable AR conical intake concepts.

decrease in the duct radius from centre to edge. Table 3 provides the performance of the three concepts for the mean conditions at the 160 km SSO with average solar conditions, evaluated with the intake panel model. It is important to note here that the fundamental form (i.e. $\eta_c = 0$) intake $C_{Dintake}$ has been calculated using the penultimate of Eq. 20 without the η_c correction, $C_{Dintake} = \bar{F}_D^{intake}/0.5\bar{\rho}_\infty \bar{v}_\infty^2 A_{ref}$, with $A_{ref} = A_{in}$. Table 3 then also gives the reflected flow term $C_{Dintake}(1-\eta_c)$. The final effective drag coefficient is then given by adding the final term of Eq. 20, normalised by $0.5\bar{\rho}_\infty$, to give $C_{Dintake}(1-\eta_c)+2\eta_c$. Note that the exterior surfaces are not included here, since these form part of F_D^{bus}. The chamber aspect ratio $AR_{chamber}$ = 1.5 and the nominal duct aspect ratio $AR_{duct} = 8.5$. This gives the variable ducts a central aspect ratio of 3.1 and outer of 14, when the length of the ducts is maintained constant. The area ratio is $A_{in}/A_{out} = 10$.

Table 3: Analysis of intake concepts

	Classical	**Var. AR**	**Var. AR 30° Conical**	**Var. AR 45° Conical**
η_c	0.37	0.45	0.43	0.39
$C_{Dintake}$	2.75	2.75	2.16	1.97
$C_{Dintake}(1-\eta_c)$	1.73	1.47	1.23	1.20
$C_{Dintake}(1-\eta_c)+2\eta_c$	2.47	2.47	2.09	1.98

With the variable aspect ratio design there is a 22% increase in η_c. Two average values of the conical angle were then considered: a 30° and 45° slope results in 4% and 13% η_c reductions respectively, but 15% and 20% reduction in total effective drag coefficient. A DSMC simulation was conducted of the 30° variable AR conical intake, using the code described in Andrews et al. [39]. The domain is 2D axisymmetric, with a Maxwellian N_2-O inflow from the left boundary (with drift velocity 7812 m/s plus density and temperature corresponding to the aforementioned mean conditions for 160 km SSO) and all other boundaries open free-flow. The latter includes the source tube exit, which corresponds to a $\Theta_{out} \approx \eta_u = 1$ validation case. The accommodation coefficient is $\alpha_w = 0.9$. From the simulation, the obtained $\eta_c = 0.44$ and $C_{Dintake}$

= 2.28 validates the use of the panel method (3% and 5% error). The steady-state number density distribution is illustrated in Fig. 6. The compression ratio in this case was found to be 68.

It is warranted to briefly discuss the physical justification of the conical intake and the relatively low values of drag coefficient observed. The conical form itself does not directly reduce the drag in the same way a conical profile does so versus a flat plate, since the intake is transparent to the flow. Instead, the collision of particles with the protruding exterior surfaces of the ducts allows for those particles, that would otherwise be trapped and detrimentally contribute to back-scattered flow, to diffuse around the intake instead. The conical profile also means that those particles which are reflected from the chamber through the ducts and contribute to back-scatter are more likely to retain some positive momentum contribution onto the direction of the incident flow. Qualitatively, this is confirmed by the reduction of the high-density bow-wave in front of the intake further up the conical section in figure 6. Finally, the variable duct widths allow for significantly more particles to pass through the intake into the source tube without losing momentum.

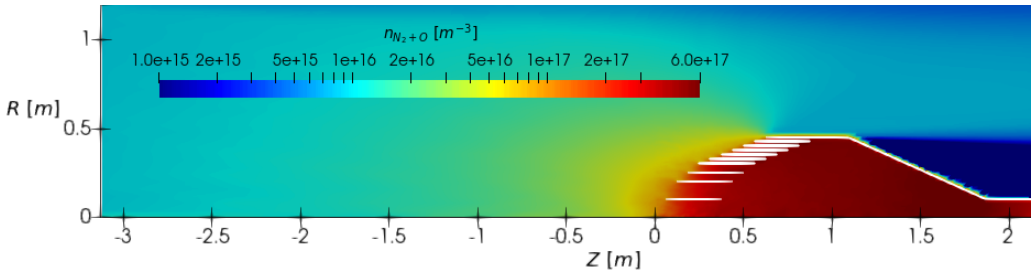

Figure 6: Total species number density n_{N_2+O} in the variable AR conical intake.

Therefore, for the purposes of the optimisation, the edge to centre duct width ratio and slope angle were fixed at 0.1 and 30° respectively. It is left to future work to include these in the optimisation procedure, as to eliminate two additional design variables.

Following the optimisation, Fig. 7 provides the pareto-optimal solutions of the intake design, where it is shown that higher performing intakes are less robust and vice-versa (in this case). The non-robust intake yields a $\overline{\eta}_c = 0.51$. One major driver of robustness is the area ratio. Larger intake areas can more easily satisfy the minimum ignition requirements for the mass flow rate that will provide sufficient neutral concentration under the RF antenna; larger mass flows also lower the electron temperature for the same power, thus safeguarding against the constraint on thermal loading. However, increased area ratio greatly reduces performance, demonstrated

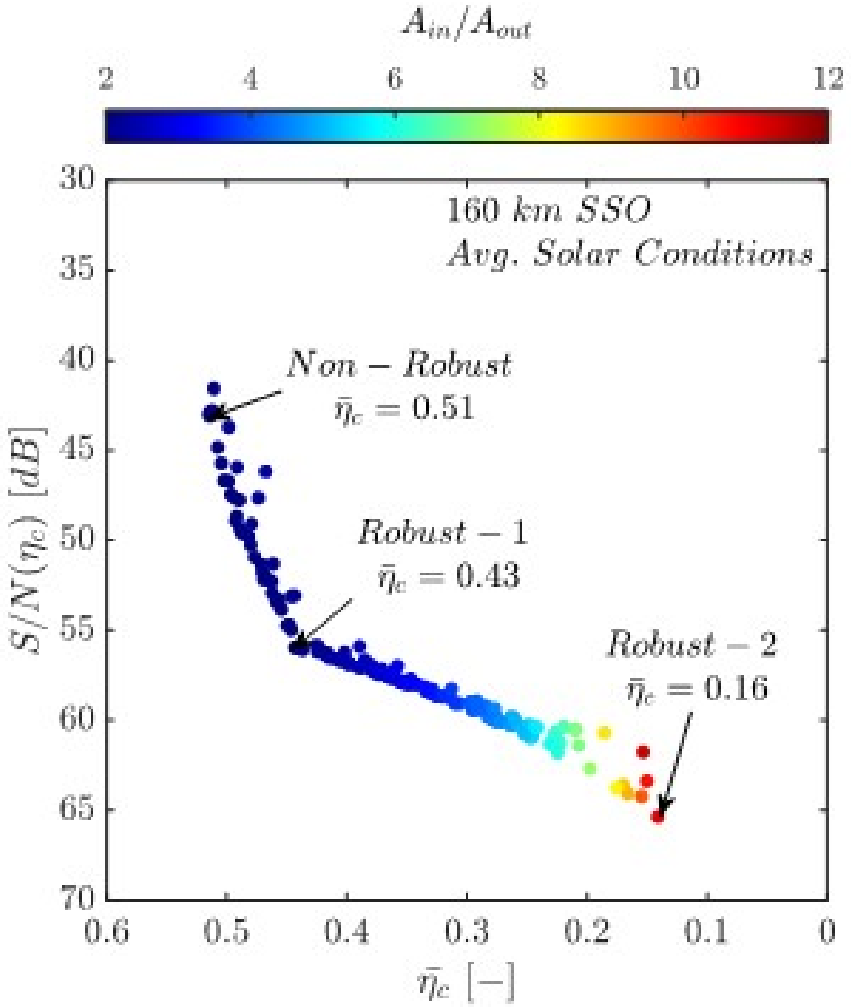

Figure 7: Pareto front of the mean collection efficiency and its SNR for 160 km SSO, average solar conditions.

by the most robust solution giving $\overline{\eta}_c = 0.16$, with $A_{in}/A_{out} = 12$. While feasible, this puts far greater requirements on thruster power to achieve a breakeven condition.

The solution chosen from the pareto front was taken to be that at the inflection point, noted as 'robust-1' on Fig. 7. This provides the median trade-off in mean performance and robustness. An average $\overline{\eta}_c = 0.43$ is yielded, a 16% reduction from the non-robust value but a 30% increase in SNR. For this case A_{in}/A_{out} =3.5, and the resultant intake is illustrated in Fig. 8.

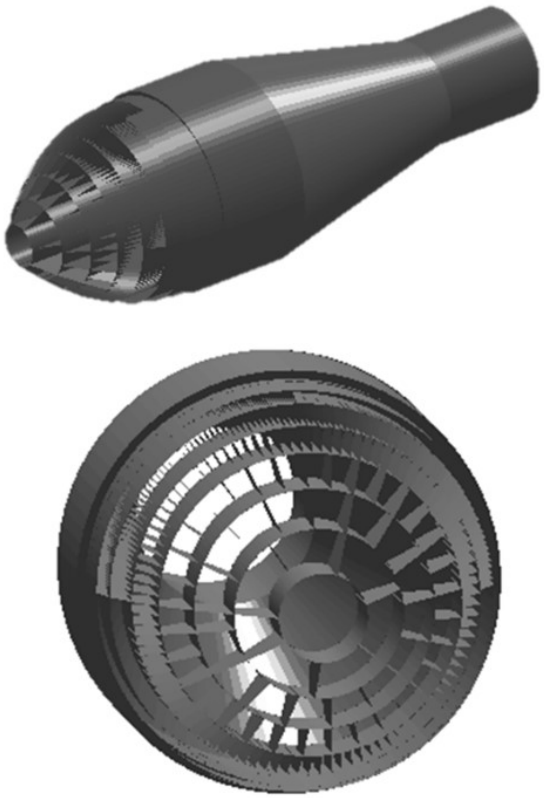

Figure 8: Rendering of the 'robust-1' intake.

4.3. Thruster performance

The corresponding 'robust-1' pareto-optimal solution is illustrated on the pareto front of thrust efficiency $\overline{\eta}_t$ in Fig. 9. There exists a linear relationship between the thrust efficiency and its SNR, but the SNR it of around half the values of the intake collection efficiency. This suggests that the air ionisation is far less forgiving to changes in the air composition than the intake is to its own noise parameters.

At the 'robust-1' point, $R_{thruster} = 0.1$ and the thruster aspect ratio is 3.4, which gives a $\overline{\eta}_t = 0.11$. Except for a cluster of high aspect ratio solutions at the region of greater mean performance, there is little relationship of $L_{thruster}/R_{thruster}$ along the front.

The characteristics of this optimal thruster are given in Fig. 10 with thrust and thrust-to-power ratio for varying absorbed power and mass flow rate. Most notable is that increased N_2 composition reduces performance up to 20%, particularly for high $\dot{m}$ or low P_a.

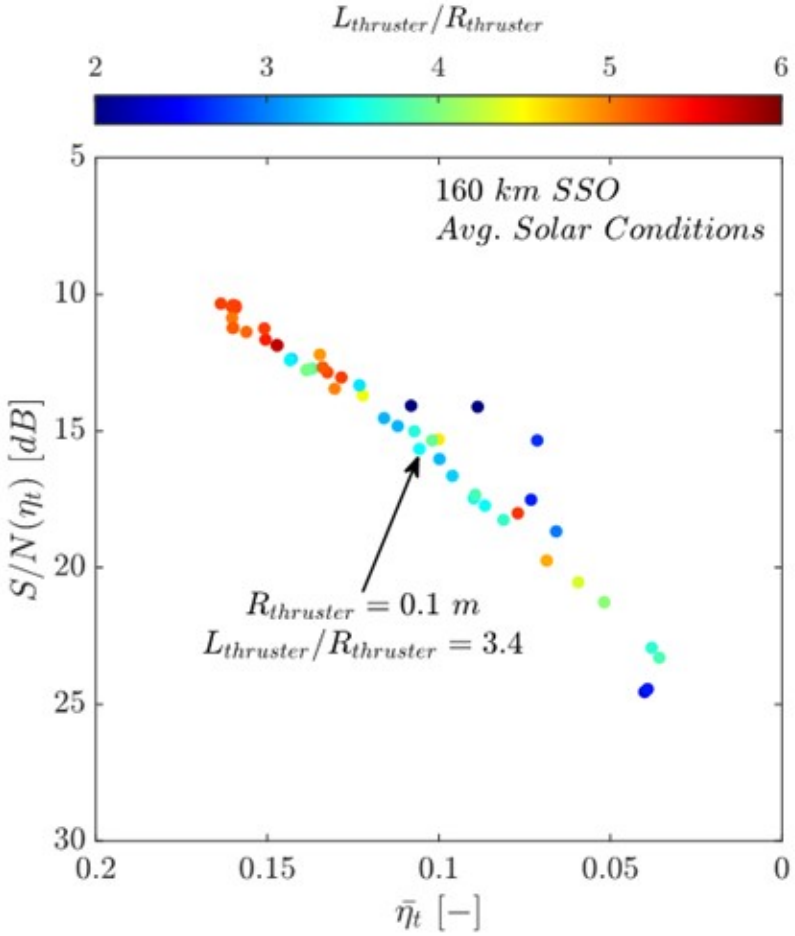

Figure 9: Pareto front of the mean thrust efficiency and its SNR for 160 km SSO, average solar conditions.

Referring to Fig. 2 (b), lower altitudes, the maximum inflow condition, tend to higher O composition. So, this characteristic is advantageous in this case. However, in general, lower mass flow rates are far more robust to composition; there is negligible performance difference with power in the case of 0.1 mg/s. This suggests that higher altitudes may be less susceptible to atmospheric uncertainty.

Overall, thrust-to-power ratios of about 15-32 mN/kW are achievable in the 150 – 500 W range, which is in-line with the performance of the REGULUS-50 and REGULUS-150 thrusters that operate on xenon and iodine propellant [26,32].

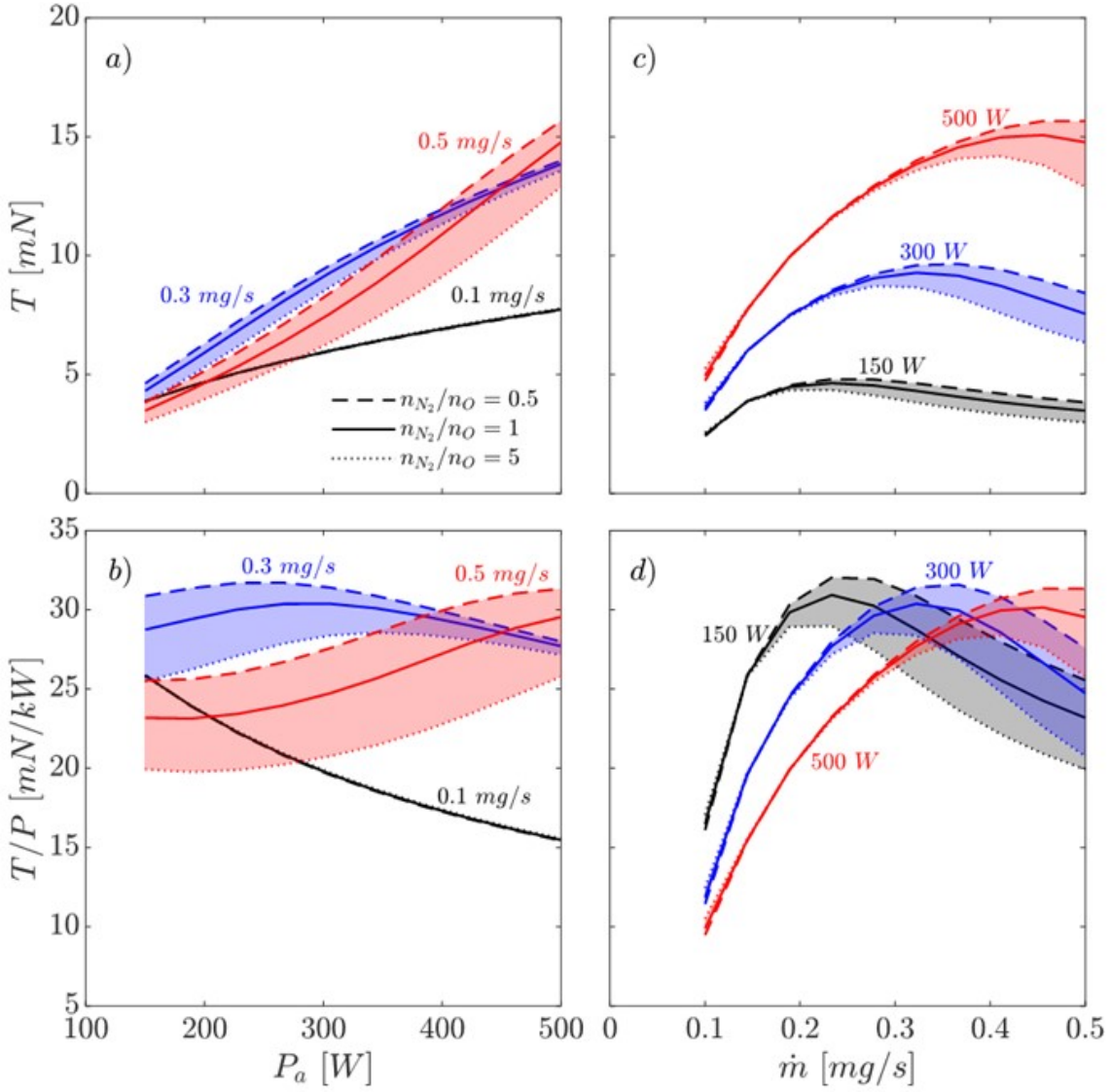

Figure 10: Thrust and thrust-to-power variation with absorbed power and mass flow rate for source tube with $R_{thruster} = 0.1$ m and $L_{thruster}/R_{thruster} = 3.4$, for varying atmospheric composition.

4.4. System performance

The Pareto fronts presented in figures 7 and 9 decomposed the final result into the constituent metrics of $\bar{\eta}_c$ and $\bar{\eta}_t$ so as to allow better insight into what drives the robust characteristics between intake and thruster. The main Pareto front for the $\eta_C \doteq c\eta_t$ optimisation criterion from Eq. 27 is therefore also given in figure 11,

which identifies the points of maximum robustness (29 dB) and maximum efficiency ($\eta_c\bar{\eta}_t = 0.16$). Comparing figure 11 to figures 7 and 9 it can be said that the shape of the Pareto front is driven primarily by the intake, whereas the overall SNR is limited by the thruster behaviour (relatively, the intake exhibits high SNR). Note, that restricting the altitude range used in this work, via some method of active orbit control, would enable higher $\eta_c\bar{\eta}_t$ solutions to be feasible. Since, according to figure 11, the SNR decrease plateaus significantly beyond $\eta_c\bar{\eta}_t \approx 0.1$, large increases in efficiency could be utilised for small sacrifices in robustness.

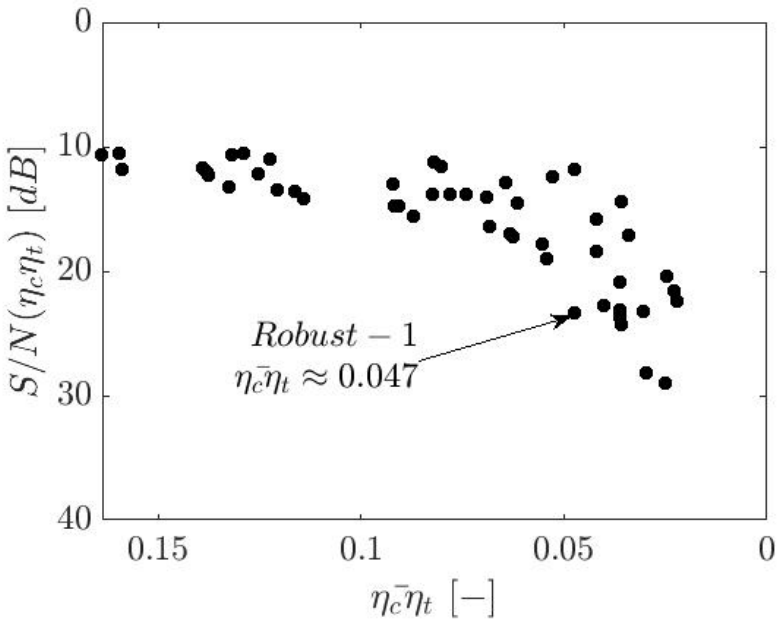

Figure 11: Pareto front of the Eq. 27 efficiency metric and its SNR for 160 km SSO, average solar conditions.

A summary of the final optimised design parameters is given in Table 4. Besides, the pareto-optimal design variables, it also provides the value of several important parameters: The mean total spacecraft drag coefficient (defined as $C_D = \bar{F}_D/0.5\bar{\rho}_\infty\bar{v}_\infty^2 A_{in}$) is 3.85, circa the 3.7 observed for the GOCE mission [5]. The majority of the drag arises from the intake, where $C_{Dintake} = 2.09$ (the final two terms of Eq. 20). The wing-mounted arrays contribute $C_{Darray} = 1.25$, and the remainder arises from the shear contributions of the satellite bus surrounding the aft intake and thruster. The total solar panel area A_s required—dictated by the maximum power condition—is 2.75 m^2, which corresponds to solar-facing wing-mounted areas of 1.17 m^2, with a 0.42 m^2 body-mounted contribution.

Table 4: Final system parameters

AR_{duct}	[-]	7.8
$AR_{chamber}$	[-]	2.1
A_{in}/A_{out}	[-]	3.5
R_{out}	[m]	0.1
$L_{thruster}/R_{out}$	[-]	3.4
$\bar{C}_D$	[-]	3.85
$\bar{C}_{Dintake}$	[-]	2.09
$\bar{C}_{Darray}$	[-]	1.25
A_s	[m^2]	2.75
$A_s - A'_{bus}$	[m^2]	2.33

The resultant system performance for 160 km SSO is then given in Table 5 for both the minimum and maximum thruster mass flow rates, which dictate the design. The minimum inflow condition is what constrains the performance. Lower mass flow rates raise the electron temperature in the source tube, which approaches the limit of thermal loading. Larger A_{in} to increase this only serves to increases drag. It must also be considered that array area is sized by the maximum inflow power of 912 W (compared to 308 W) which further demand on the minimum inflow condition.

Table 5: Final system performance

	$\dot{m}_{out}$ [mg/s]	T/D	P_a [W]
Minimum $\eta_c \rho_\infty v_\infty$	0.11	1.03	308
Maximum $\eta_c \rho_\infty v_\infty$	1.02	1.47	912

In accordance with the criteria for sustained VLEO flight laid down by Filatyev et al. [46], it can be confirmed that at minimum inflow, where $\eta_c = 0.15$, that $T\eta_c/\dot{m}_{out}v_\infty \approx 1$, which lends good credibility that the optimiser has found a bounding constraint. A T/D ratio of just 1.03 is not a reassuring result. Therefore, it is possible that further detailed design may have to consider a form of station-keeping within the ABEP mission to control the range of orbital altitude to relieve the minimum inflow constraint. Given that a T/D of 1.47 is obtainable at maximum inflow, it is apparent that such surplus ΔV station-keeping will be available; especially since reducing the variability of atmospheric conditions by constraining altitude should increase the mean thrust-to-drag ratio. It should be highlighted also that the array

sizing in this work can be regarded as highly conservative. Section 3.4 not only considered a 10-year photovoltaic degradation, but also a power supply safety factor of 1.2.

The case study presented here has considered solely the 160 km SSO at average solar conditions. Since it has been seen that the minimum inflow condition largely constrains the design, it is prudent to consider the sensitivity of the final system design parameters to a reduction in the solar activity. Whilst reduced free-stream density at low solar activity reduces the drag by approximately 20%, this is balanced by the reduction in minimum inflow of around 13% (η_c increases to 0.47). With small propellant flow reduction compared to drag reduction, it would seem at first that the solution is to simply throttle down the thruster power to achieve a break-even condition. However, as power is reduced, so too is the mass utilisation efficiency $\eta_u \approx \Theta_{out}$. As per Eq. 14, reducing Θ_{out} greatly reduces η_c and thus no feasible condition exists. The model was therefore run for a series of lower SSO orbits, where it was found that, in order maintain stable VLEO flight at low solar activity, the final system would require a new 153 km SSO, a 7 km mean altitude reduction. It is interesting to note that despite the large increase in atomic oxygen relative to diatomic nitrogen under low solar activity (see Fig. 1 (b)) that this is partly alleviated by the natural increase of diatomic nitrogen at lower altitude. At the lower mass flow rates experienced at the minimum inflow condition ($\mathcal{O}(0.1)$ mg/s) though, the thruster performance is largely insensitive as seen in Fig. 10. This is primarily because lower flow rate conditions see higher electron temperatures (T_e >15 eV) within the source tube, at which the effective collisional energy loss of oxygen and diatomic nitrogen are similar.

5. Conclusions

This paper has presented the preliminary feasibility analysis and optimisation of an atmosphere-breathing electric propulsion (ABEP) system based on cathode-less radio frequency (RF) plasma thruster technology. A global model of air plasma, accounting for the complex reactions and energy loss pathways of molecular chemistry forms the basis of a system model to allow low fidelity evaluation of performance for many design variables.

A novel intake concept has been introduced, which combines variable aspect ratio ducts with a conical frontal silhouette to both increase collection efficiency and reduce drag. The cathode-less RF plasma thruster demonstrates T/P = 15-32 mN/kW, comparable to the REGULUS technology from which it is based.

The constraining aspect to ABEP performance is the minimum inflow condition,

where the electron temperature limit imposed by thermal loading result in breakeven condition just above 1.

Future work will include a move to higher-fidelity design tools such as Direct Simulation Monte-Carlo (DSMC) for the intake, and fluid [40,41] and Particle-in-Cell (PIC) codes [39,42] for the plasma source and magnetic nozzle respectively. The optimisation procedure will also be extended to multiple altitudes and orbital profiles to further interrogate the feasibility beyond the 160 km sun-synchronous orbit (SSO) case considered here. An investigation is also warranted into the interactions of the plasma plume with the oncoming flow [43,44], which may impact thrust generation in the magnetic nozzle.

Nonetheless, the robust methodology presented here highlights a major aspect of ABEP design. That is, to account for atmosphere variations and uncertainties to deliver improved feasibility, reliability, resilience, and adaptability. The models enable quick and reliable trade-off, regardless the uncertainty of mission constraints, opening the possibility to conduct studies on potential spacecraft integration.

References

[1] S. Vaidya et al. Development and analysis of novel mission scenarios based on Atmosphere-Breathing Electric Propulsion (ABEP), CEAS Space J. 14 (2022), 689–706.

[2] J. Virgili-Llop et al., Very Low Earth Orbit mission concepts for Earth Observation. Benefits and challenges. Reinventing Space Conference, London, UK, 18–21 November 2014.

[3] N. Crisp et al., The benefits of very low earth orbit for earth observation missions, Prog. Aerosp. Sci., 117 (2020), 100619

[4] L. Berthoud et al. Are Very Low Earth Orbit (VLEO) satellites a solution for tomorrow's telecommunication needs? CEAS Space J. 14 (2022), 609-623

[5] G. Sechi et al. In-Flight Results from the Drag-Free and Attitude Control of GOCE Satellite, IFAC Proceedings Volumes, 44(1) (2011), 733-740

[6] K. Fujita and A. Noda, Aerodynamics of Satellites on a Super Low Earth Orbit, in AIP Conference Proceedings, Kyoto, 2008

[7] D. Di Cara et al., RAM Electric Propulsion for Low Earth Orbit Operation: An ESA study. 30th International Electric Propulsion Conference, Florence, Italy, 17–20 September 2007.

[8] K. Nishiyama, A Study of Air Breathing Ion Engine. Space Technol. Jpn. Jpn. Soc. Aeronaut. Space Sci. 4 (2005), 21–27

[9] T. Andreussi et al. The AETHER project: development of air-breathing electric propulsion for VLEO missions, CEAS Space Journal, (2022).

[10] K. Hohman, Atmospheric Breathing Electric Thruster for Planetary Exploration. NIAC Spring Symposium, Pasadena, CA, 27–29 March 2012.

[11] B. Banks, S. Miller and K. de Groh. Low Earth Orbital Atomic Oxygen Interactions with Materials, AIAA 2004-5638. 2nd International Energy Conversion Engineering Conference. August 2004.

[12] F. Romano et al., System analysis and test-bed for an atmosphere-breathing electric propulsion system using an inductive plasma thruster, Acta Astronaut.147 (2018), 114–126.

[13] M. Manente, et al., REGULUS: A propulsion platform to boost small satellite missions, Acta Astronautica, 157 (2019) 241-249.

[14] M. Duzzi et al., E-REGULUS: development of a 150 W prototype of magnetically enhanced plasma thruster, IAC-21-C4.5.9, 72nd International Astronautical Congress, Dubai, UAE, 2021.

[15] D. Rafalskyi et al., In-orbit demonstration of an iodine electric propulsion system., Nature 599 (2021) 411–415.

[16] N. Bellomo, M. Magarotto, M. Manente et al., Design and In-orbit Demonstration of REGULUS, an Iodine electric propulsion system, CEAS Space J 14 (2022) 79–90.

[17] N. Bellomo et al., Enhancement of microsatellites' mission capabilities: integration of REGULUS electric propulsion module into UniSat-7, IAC-19-C4.8-B4.5A.5, 70th International Astronautical Congress, Washington D.C., USA, 2019.

[18] K. Takahashi, Helicon-type radiofrequency plasma thrusters and magnetic plasma nozzles, Reviews of Modern Plasma Physics, 3(1) (2019) 1-61.

[19] M. Magarotto, D. Pavarin, Parametric study of a cathode-less radio frequency thruster, IEEE Transactions on Plasma Science, 48(8) (2020) 2723-2735.

[20] C. Rapisarda et al., Design and optimisation of a passive Atmosphere-Breathing Electric Propulsion (ABEP) intake, Acta Astronautica, 202 (2023),77-93

[21] F. Romano et al., Intake design for an Atmosphere-Breathing Electric Propulsion System (ABEP), Acta Astronautica, 187 (2021), 225-235.

[22] S. Dalle Fabbriche et al., Development of a Global Model for the Analysis of Plasma in an Atmosphere-Breathing Cathode-Less Thruster, Aerospace 10 (2023), 389.

[23] J. Picone, A. Hedin, D.P. Drob and A. Aikin, NRLMSISE-00 empirical model of the atmosphere: Statistical comparisons and scientific issues, J. Geophys. Res. Space Phys. 107 (A12) (2002) SIA– 15.

[24] M. Magarotto et al., Numerical suite for cathodeless plasma thrusters, Acta Astronautica, 197 (2022) 126-138.

[25] M. Magarotto et al., Numerical Suite for Magnetically Enhanced Plasma Thrusters, IAC-21-C4.6.3, 72nd International Astronautical Congress, Dubai, UAE, 2021.

[26] S. Andrews et al., Coupled global and PIC modelling of the REGULUS cathodeless plasma thrusters operating on xenon, iodine and krypton, Acta Astronautica, 207 (2023), 227-239.

[27] M. Guatia et al., Semi-analytical model of a helicon plasma thruster, IEEE Transactions on Plasma Science, 50(2) (2022) 425-438.

[28] T. Lafleur, Helicon plasma thruster discharge model, Phys. Plasmas,21(4) (2014), 043507

[29] LXcat, The Plasma Data Exchange Project. Available online: https://nl.lxcat.net (accessed on 2 September 2023

[30] E. Majorana et al., Development of a Plasma Chemistry Model for Helicon Plasma Thruster analysis, Aerotecnica Missili & Spazio, 100(10) (2021).

[31] N. Souhair, M. Magarotto, E. Majorana, F. Ponti, D. Pavarin, Development of a lumping methodology for the analysis of the excited states in plasma discharges operated with argon, neon, krypton and xenon, Physics of Plasmas, 28(9) (2021).

[32] N. Souhair, M. Magarotto, S. Dalle Fabbriche, R. Andriulli, S. Andrews et al., Simulation and modelling of an iodine fed Helicon Plasma Thruster, IEPC-2022-496, 37th International Electric Propulsion Conference, Cambridge, MA, USA, 2022.

[33] S. Zhang et al., Mechanism of capture section affecting an intake for atmosphere-breathing electric propulsion, Chinese Journal of Aeronautics, 2023.

[34] F. Romano et al., Air-Intake Design Investigation for an Air-Breathing Electric Propulsion System, 34th International Electric Propulsion Conference, Kobe, Japan, 2015.

[35] L. Sentman, Free molecular flow theory and its application to the determination of aerodynamic forces, Technical Report LMSC-448514, Lockheed Missiles and Space Co., Sunnyvale, CA, 1961.

[36] C. He at al., A review of surrogate-assisted evolutionary algorithms for expensive optimization problems, Expert Systems with Applications, 217 (2023), 119495.

[37] G. Taguchi, 1986. Introduction to Quality Engineering, Asian Productivity Organization (Distributed by American Supplier Institute Inc., Dearborn, MI).

[38] R. Unal and E. Dean, Taguchi approach to design optimization for quality and cost: An overview, Annual Conference of the International Society of Parametric Analysts, 1991.

[39] S. Andrews, S. Di Fede, M. Magarotto, Fully kinetic model of plasma expansion in a magnetic nozzle, Plasma Science Sources and Technology, 31 (2022) 035022.

[40] M. Magarotto, D. Melazzi, D. Pavarin, 3D- VIRTUS: Equilibrium condition solver of radio- frequency magnetized plasma discharges for space applications, Computer Physics Communications, 247 (2020) 106953.

[41] N. Souhair et al., Analysis of the plasma transport in numerical simulations of helicon plasma thrusters, AIP Advances, 11(11) (2021) 115016.

[42] S. Di Fede, M. Magarotto, S. Andrews, D. Pavarin, Simulation of the plume of a magnetically enhanced plasma thruster with SPIS, Journal of Plasma Physics, 87(6) (2021) 905870611.

[43] S. Andrews and L. Berthoud, Characterising Satellite Aerodynamics in Very Low Earth Orbit inclusive of Ion Thruster PlumeThermosphere/Ionosphere Interactions, Acta Astronautica, 170 (2020), 386-396.

[44] S. Andrews and L. Berthoud, Effect of Ion Thruster Plume-Thermosphere Interaction on Satellite Drag in Very Low Earth Orbit. 70th International Astronautical Congress, Washington D.C., USA, 2019.

[45] J. Walsh et al., Drag Reduction through Shape Optimisation for Satellites in Very Low Earth Orbit. Acta Astronautica, 179 (2021) 105-121.

[46] A. Filatyev et al., Research and development of aerospace vehicles with air breathing electric propulsion: Yesterday, today, and tomorrow. Progress in Aerospace Sciences. 136 (2023).

Highlights

Cathode-less RF Plasma Thruster Design and Optimisation for an Atmosphere-Breathing Electric Propulsion (ABEP) System

- Cathode-less RF thruster: reduced erosion issues, enhanced reliability
- Global air chemistry model facilitates conceptual design review
- Multidisciplinary robust optimisation considers atmospheric variability
- Novel passive intake introduced which yields 43% collection efficiency with reduced drag
- Preliminary 15-32 mN/kW achievable for 160 km sun-synchronous orbit case study